Predicting interlaminar damage behaviour of fibre-metal laminates containing adhesive joints under bending loads

Ahmad S.M. Al-Azzawi [1,3*], L.F. Kawashita [2], C.A. Featherston[1]

[1] *School of Engineering, Cardiff University, The Parade, Cardiff, CF24 3AA, UK*
[2] *Bristol Composites Institute, University of Bristol, Bristol, BS8 1TR, UK*
[3] *College of Engineering/Al-Mussaib, University of Babylon, Babylon, Iraq*
[*]Corresponding author: Email address. msb.ahmed.s@uobabylon.edu.iq

Keywords: Bending, Delamination, Cohesive zone model, Adhesive joints, Fibre- metal laminates, Friction and shear enhancement, through-thickness compressive stresses

Abstract

This study includes experimental and numerical investigations on fibre-metal laminate structures containing adhesive joints under static bending loads. Experimental tests were carried out on Glare® 4B specimens manufactured in-house and containing doubler joint features. Numerical analyses were performed using Abaqus software including damage in the glass fibre reinforced polymer (GFRP) layers, ductile damage in the resin pockets (FM94 epoxy) and the plasticity in the metal layers. A new cohesive zone model coupling friction and interfacial shear under through-thickness compressive stress has been developed to simulate delamination initiation and growth at the metal/fibre interfaces with the adhesive joint under flexural loading. This model is implemented through a user defined VUMAT subroutine in the Abaqus/Explicit software and includes two main approaches, firstly, combining friction and interfacial shear stresses created in the interlaminar layers of the fibre-metal laminate as a result of through-thickness stresses and secondly, considering elastic-plastic damage behaviour using a new cohesive zone model based on the trapezoidal law (which provides more accurate results for the simulation of toughened epoxy matrices than the commonly used bilinear cohesive zone model). Numerical results have been validated against experimental data from 4-point bending tests and a good correlation observed with respect to both crack initiation and evolution. Delamination and shear failure were noted to be the predominant failure modes under bending stresses

as expected. This is due to the higher mode-II stresses introduced during bending which cause different damage evolution behaviour to that seen for axial stresses. Finite element results revealed that both friction and shear strength parameters generated from through-thickness compression stresses have a significant effect in predicting damage in fibre-metal laminate structures under this type of loading.

1. Introduction

The Fibre Metal Laminate (FML) Glare® is manufactured from aluminium sheets and glass fibre reinforced polymer composite layers. Glare has several advantages over CFRP's including improved impact, fire and corrosion resistance, and increased damage tolerance which leading to its increased commercial use for example in aircraft structures such as the fuselage [1,2]. Despite its advantages however, Glare's complex structure brings additional challenges in terms of understanding its multiple damage mechanisms. A fuselage for example is required to withstand multiple flight stresses. One of the main stresses is the static bending stress. Several studies have been conducted considering static bending on FMLs, using both three-point and four-point bending tests. When FMLs are subjected to bending, shear and bending act simultaneously, resulting in both shear and normal stresses acting on a transverse section. In terms of the normal stresses, one side of the laminate is subject to a tensile stress, whilst the other is under compression. As the deflection increases, the laminate continues to bend and deform. When the bending deformation reaches the strain limit, fibre plies or metal layers may fail, resulting in bending failure. Due to different ply orientations in the composite plies included in FMLs, different failure behaviours are seen depending on the applied loads. **Liu *et al.*** [3] studied a curved section of Glare presenting SEM images of the metal/fibre interfaces for three different ply angles. As the bending stress increased, the area around the point of load application was subjected to an increasing level of compressive stress. As the metal layer began to yield, the fibre layer remained elastically deformed, but as the stress continued to increase, a high level of fibre breakage was seen. When the bearing limit was reached, interlaminar delamination failure occurred at the metal/fibre interface. After studying the bending properties of Glare laminates,

Xu [4] concluded that the difference between unidirectional and cross-ply laminates was that the cross-ply laminates not only had damage in the 0^o plies but also suffered crack expansion in the 90^o plies. When the stress limit was reached, interlaminar delamination failure occurred. If the stress continued to increase, it eventually led to metal breakage. **Ye *et al.*** [5] analysed hybrid composite structures using multiscale modelling. They found that cracks first appeared in the 90^o layers, but as the external load continued to increase, cracks accumulated in the ply direction for -45^o, $+45^o$ and 90^o plies. **Hu** [6] found a similar result when studying Ti/CF/PMR polyimide super-hybrid laminates. Under bending stress, the main failure modes were delamination failure and local buckling. Delamination or debonding is one of the most common failure mechanisms in composite structures. It occurs mostly at the metal/fibre interfaces [7]. As the stress increases and the fibres deform along their length, they are gradually be pulled out [8]. Interfacial debonding and fibre pull-out of FMLs are issues of great concern, which interact with each other and ultimately lead to material failure. There are many factors affecting debonding and delamination, including interlaminar shear stresses, differences in properties, stress type, stress increment and the bonding strength of different material interfaces. FMLs with insufficient rigidity and poor interlaminar shear strength buckle easily and lose stability when subjected to shear stress. Extrusion-shear failure occurs under small support span-to-thickness ratio, resulting in debonding and delamination at multiple interfaces [9]. **Liu** found that when a Glare laminate had a support span-to-thickness ratio of 8, interlaminar shear failure occurred, leading to local shear debonding at the metal/fibre interfaces, while, if the supports span-to-thickness ratio was greater than 10, the failure mode was bending failure. Interlaminar delamination in FMLs is typically caused by normal peeling stress and the low shear strength of the materials. It is often accompanied by delamination. Once delamination occurs, structural stiffness and strength and in particular, compressive strength will be significantly reduced [10]. Notched FMLs have also been studied by some researchers, with [11] using X-ray radiography scans to inspect delamination profiles in notched FML specimens, after the aluminium layers of fractured samples were chemically removed. It was found that the notch sizes not only influenced the strength but also affected the size of the delamination. **Carrillo and Cantwell** [12], studied the flexural static strength of Glare laminates using

a 4-point bending test with different GFRP layups, [±45°] and [0°/90°]. They noticed that neither type of specimen failed before reaching the maximum bending load and that considerable out-of-plane deformation was observed without apparent damage. Closer inspection highlighted the lack of any delamination at the metal/fibre interfaces, where it was noted that none of the constituents in the FML had failed during testing. **Jung *et al.*** [13] examined the bending performances of aluminium–GFRP hybrid square tube beams experimentally and compared the results with those from a virgin aluminium beam. They concluded that the hybrid tube beams which were cured with an adhesive film inserted between the aluminium and composite layers suppressed the delamination. A three-point bending test was conducted on FMLs with two different types of glass fibre reinforced plastics and different aluminium layers thickness in [14]. It was concluded that using thicker aluminium layers in FMLs gives them a higher resistance to bending when comparing to lower thicknesses. Experiments also showed that the aluminium layers failed first when combined with high out-of-plane strength glass fibre layers (CSM). **Rajkumar *et al.*** [15], investigated the static bending behaviour of FMLs incorporating both GFRP and CFRP laminates and observed that flexural failure was mostly as a result of delamination at the aluminium/fibre interfaces for both types of composite. A numerically based constitutive model was developed in [16] to predict the progressive failure of FMLs under both tension and bending loads. This included an elasto-plastic model with a 3D ductile damage criterion, an elastic model with a 3D continuum damage criterion and a cohesive model with a 3D delamination criterion. It was found that the strains and stresses at the neutral surfaces were remained almost the same regardless of fibre orientation. Fibre orientation affects the FML's properties by controlling strain and stress gradients. The growth of fibre breakages and matrix cracks occurred parallel to the fibre orientation. Delamination occurred prior to the failure of the fibre layers and along the fibre orientation. Interlaminar delamination in CFRP/aluminium laminates (CARRAL) was modelled by employing the cohesive tiebreak algorithms available in LS-Dyna [17]. The tie-break contact algorithm which is based on a bilinear constitutive traction-separation law, prevents interpenetration between the slave and master surfaces due to the removal of tensile coupling. Three-point bending tests were carried out on two material systems made of CARRAL.

Predicted FE results presented a remarkable agreement with experimental results. **Mansourinik *et al.*** [18], studied the behaviour of sandwich hybrid beams consisting of a PVC foam core and twill-woven E-glass composite skins with and without initial core–skin debonding under flexural loads through numerical and experimental procedures. The cohesive zone model and the extended finite element method were utilized successfully to capture crack initiation and propagation at the core–skin interfaces as well as inside the foam core. **Fallahi *et al.*** [19] presented a comprehensive review of the nonlinear mechanical behaviour of polymer matrix composites (PMCs). Following an increasing degree of complexity, models were categorized into four major classes: nonlinear elasticity models, elastic-plastic models, elastic-plastic viscous models and Damage-Plasticity models with the vast number of existing models primarily due to the anisotropy and inhomogeneity of PMCs. More recently **Azhdari *et al.*** [20] carried out numerical and experimental studies to investigate damage initiation and evolution in FMLs subject to low velocity impact. In-house manufactured Glare specimens were subject to different impact energy levels. Optical microscopy (OM) and scanning electron microscopy (SEM) were then used to investigate microstructural damage in the specimens and with results revealing that the first crack occurred in the lower aluminium layer at 18.5 J. Experimental results were validated using a numerical model implemented in the ABAQUS/Explicit solver with a VUMAT user-defined subroutine including the three-dimensional Hashin damage initiation and evolution models. Furthermore **Bellini** [21] investigated the Interlaminar Shear Strength (ILSS) of both GFRP and Glare laminates through a three-point bending test carried out on short beam specimens. From the experimental results, a slightly higher strength was found for the GFRP laminate, although the difference was at a level similar to experimental scattering. Taking into account the CoVs (Coefficients of Variation) which are 2.69% for GLARE and 14.92% for GFRP the ILSS obtained for the two different materials could be considered almost comparable.

Although many studies have been performed considering the bending behaviour of FML structures as described above, the effect of friction and enhanced shear strength caused by through-thickness compression has not been considered. Recent studies on composite structures ([22-33]) however, have revealed that including through-thickness compression stresses in

cohesive zone models for interlaminar damage behaviour results in significant improvements in simulation results when compared with experiments for structures subjected to similar loading effects such as biaxial loading, low velocity impact and bending loads. **Hassan Ijaz *et al.*** [22], developed an inelastic damage model in order to simulate damage in Z-pinned laminated composite structures with friction effects. The main idea of this work was the modification of the strain energy parameter by the introduction of sliding and friction parameters. Results for single Z-fibre pull tests showed good correlation with the proposed model for micro-scale predictions. A novel rate-dependent mode-I CZM combining damage-mechanics with fractional viscoelasticity was presented by **Musto and Giulio Alfano** [23]. The criterion used in the model relies on the assumption that the measured fracture energy is the sum of a rate-independent 'rupture' energy, related to the rupture of primary bonds at the atomic or molecular level, and an additional dissipation caused by other rate-dependent dissipative mechanisms present in the material and occurring simultaneously to rupture. The model matched well with experimental results for the case of a DCB specimen made of two steel arms bonded along a rubber interface. A new cohesive zone model was developed by **Zou and Hameed** [24]. Their approach uses a cohesive energy related parameter to combine interface damage and friction and is independent of the interface stiffness. The FE results for the proposed model have been validated against experimental results for DNS tests implemented on IM7/8552 UD CFRP specimens tested under quasi-static loading using through-thickness compression stresses available in the literature, and the FE results for this model show excellent agreement with experimental results. Another approach to interfacial damage modelling including friction effects is presented by [25]. This model assumes a thin adhesive layer whose behaviour is analogous to cohesive zone models. An isotropic friction behaviour is proposed simulate solid contact behaviour and simplified numerical examples demonstrate its validity. Further numerical investigations on the influence of compressive through-thickness stresses on mode-II damage evolution have been conducted in [26]. These analyses included three different damage models based on a bilinear CZM criterion used to simulate mode-II crack propagation under through-thickness compressive stresses. The new model utilised an enhanced interlaminar shear strength parameter to reflect the effect of through-thickness compressive stresses on

interlaminar shear strength (ILSS) leading to an enhanced mode-II fracture energy G_{IIc} for the cohesive interfaces. The new failure criterion was used in the simulation of different features (cut-ply, dropped-ply and single-lap). All FE models achieved excellent correlation with experimentally found failure stresses. Both experimental and numerical investigations were implemented to simulate the interaction between compressive through-thickness stress and the out-of-plane shear at which delamination initiates in composite materials in [27]. FE analyses based on user defined interface elements and conducted considering the effect of compression enhancement allowed the experimental results to be accurately predicted. A cohesive frictional-contact model was presented by **Baek and Park** [28]. Their model integrated a cohesive zone model and a frictional-contact model to predict fracture behaviours under compression. Frictional force was approximated using a Coulomb frictional model, which accounts for the stick/slip condition. Numerical results were validated against both an earthquake rupture and masonry shear tests under compression with good agreement attained in both cases. Another modified model was proposed to include both friction and enhanced interfacial shear strength in a cohesive zone model in [29]. A bilinear traction-separation CZM with a through-thickness compression stress effect were employed to simulate delamination failure in IM7/8552 UD CFRP composite laminates using double notch specimens (DNS). Numerical predictions were in a good agreement with the available experimental data in the literature. Furthermore, a new cohesive zone model based on a thermal parameter was adopted [30]. Thermal stress was added to the Helmholtz free energy density in order to derive a new approach to incremental damage which included the effect of temperature. The developed damage model was implemented in Abaqus using a UMAT subroutine and applied to two different types of specimen. The simulation results revealed that the total energy of the interface element of high strength CFRP increased as its temperature decreased. The load-displacement curves obtained from the numerical model for both of the specimen types tested were in a good agreement with experimental data available in literature. A nonlinear cohesive/frictional contact coupled model for the mode-II shear delamination of adhesive composite joints was developed by **Liu *et al.*** [31]. A new approach combining both interface shear damage and friction in a cohesive-zone model was proposed by **Serpieri and Alfano** [32] and then verified against

experimental results for low-velocity impact, taking into consideration both the interlaminar shear and through-thickness compression stresses. The proposed model presented excellent agreement with the experimental results for all investigated cases. More recently, **Hameed *et al.*** [33] presented a new strain based constitutive damage model for simulating intra-laminar damage in composite structures. The effects of both friction coefficient and enhancement factor on the delamination failure were introduced to the proposed CZM. Using a shear enhancement factor of 0.75, and a friction coefficient of 0.5, delamination in composite laminates with different layups subject to impact tests available in the literature was successfully captured by the proposed model.

In this study, the lack of research including friction and shear enhancement parameters under through-thickness compression stresses on FMLs is addressed. Through-thickness stresses resulting from the application of 4-point bending loads and the resulting damage initiation and evolution behaviour in the interlaminar layers of Glare4B doubler specimens have been investigated using both experimental and numerical techniques. A new cohesive zone model based on strain energy release rate including both friction and enhanced shear strength stresses has been adopted. The developed damage model has been implemented in the software Abaqus® using the VUMAT subroutine and used to simulate bending tests on Glare laminates.

2. Experimental work

2.1 Specimen design

A series of specimens were tested under static bending. Specimens measured 100 mm × 13.5 mm (unsupported area during testing 80 mm × 13.5 mm) and incorporated a doubler joint inserted in the middle (Figure 1). The ratio of the support span-to the specimen's average thickness was approximately 32:1 according to the recommended value from the ASTM standards D7264/D7264M-07. They were manufactured in-house from Glare 4B and had 4 layers of aluminium alloy 2024-T3, 0.4 mm thickness and 3 layers of UD-S2 glass fibre reinforced epoxy (GFRP) prepreg (3 plies with the layup [$90^o/0^o/90^o$] according to the standard for commercial Glare [1]) on the right-hand side and

3 layers of aluminium alloy and 2 layers of GFRP on the left-hand side. The curing thickness for the GFRP plies was 0.127 mm per ply.

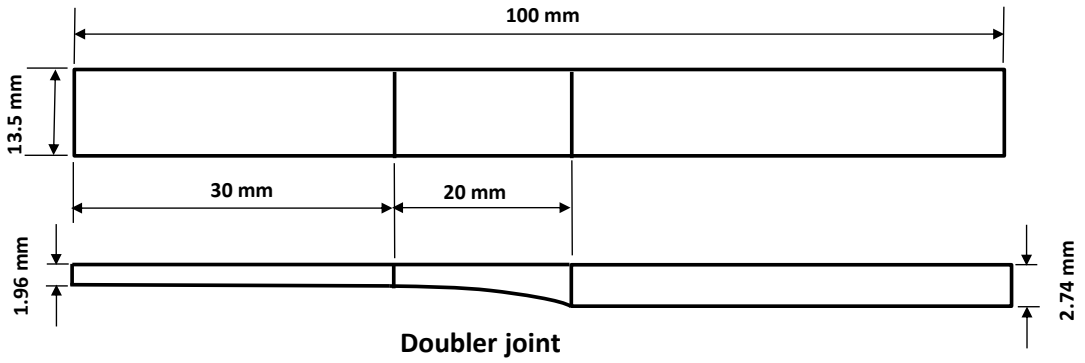

Figure 1: Glare 4B doubler specimen for flexural test.

2.2 Test rig

A test rig was designed and manufactured in-house and used for the 4-point bending test on the 4B specimens according to the ASTM standard D7264/D7264M–07 [34], as shown in Figure 2.

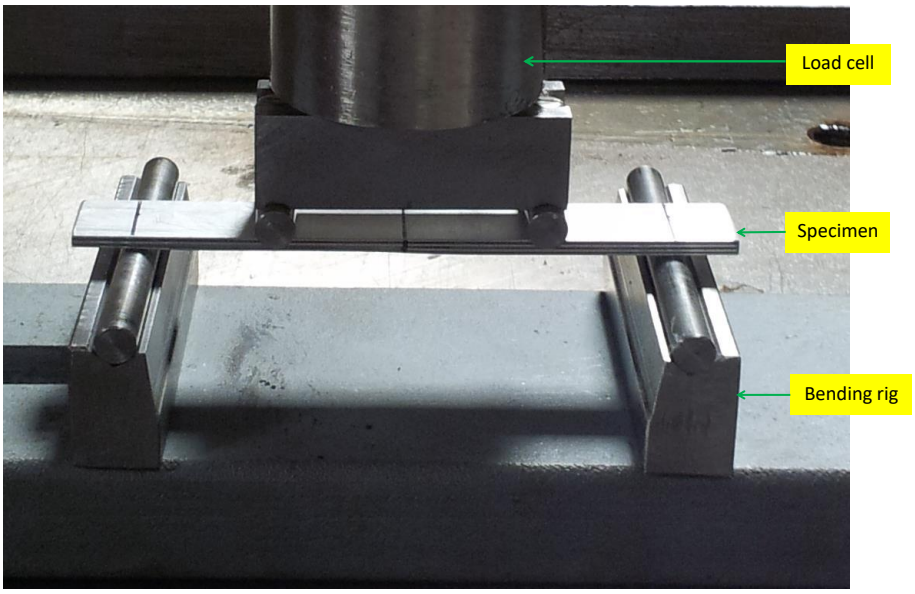

Figure 2: Four-point bending test rig.

A support span of 80 mm with a load span of half this distance was used for the rig design (Figure 3). Two steel pins 6 mm in diameter were attached to the

upper loading beam at equal distances from the centre of the beam in order to divide the load into two equal values (P/2) on each point of the load span. 25 mm high supports were used to allow for the potentially large deflections at high load which might occur as a result of plastic deformation in the aluminium layers of the Glare 4B specimen. Two steel pins of 6 mm diameter were fixed to the lower support beam at equal distances from the centre in order to support the specimen uniformly.

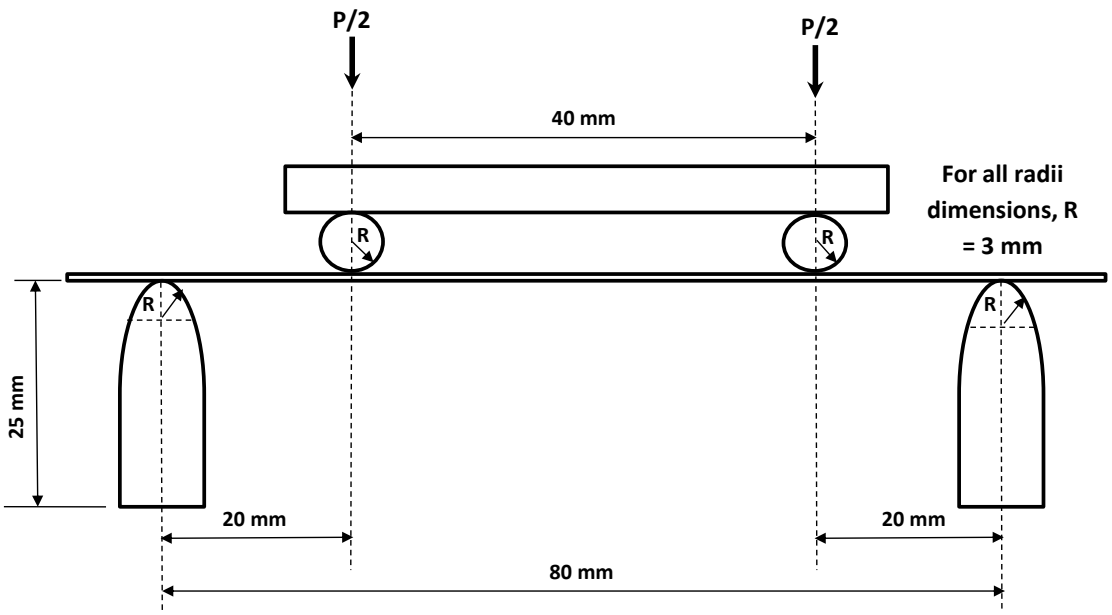

Figure 3: Schematic of the support and load spans of the four- points flexural test.

2.3 Static bending test

Four specimens were tested. Tests were performed on a 50 kN Zwick®/Roell® machine (Figure 5) under displacement control at a rate 0.01 mm/sec. Specimens were tested in the orientation shown in Figure 1 with the doubler feature facing downwards. The average maximum bending force for the four specimens was 763 N. Strain was monitored using the strain gauges on the top and bottom surfaces enabling deflection to be calculated.

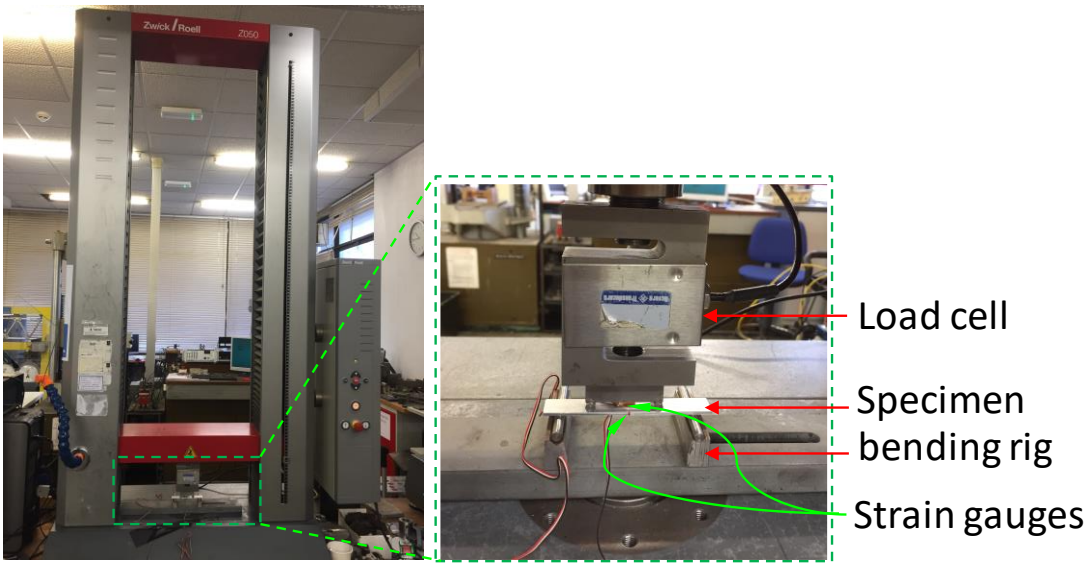

Figure 5: Experimental 4-point bending test setup.

2.4 Monitoring

Two half-bridge 250UW Vishay® microstrain gauges were used to measure the strain on the top and bottom surfaces of the doubler specimens (the configuration of these gauges is given by Figure 4). These are general-purpose gauges for narrow geometries with an overall length of 10.54 mm and gauge length 6.35 mm and both overall and grid width 3.05 mm. They were bonded to the surfaces of the specimen with an EB-2 silicone adhesive. The top strain gauge was subject to compression while the bottom gauge was under tension. An average microstrain was calculated from the two gauges and used to extract the deflection required to plot the load-deflection curve for the test. Gauges were connected to a strain indicator after setting the gauge factor (GF) for each (in this case 2.2 in tension and 1.8 in compression [35]). A *System 8000* from Micro-Measurements® was used as a strain indicator. This system includes a scanner with 8 channels of data acquisition. Strain gauge channels accept full, half or quarter-bridge configurations and have the required bridge completion components for 120 Ω, 350 Ω, and 1000 Ω bridges. Micro-Measurements StrainSmart® software is used to configure, control, and acquire data from the System 8000. Scanning rates are 1000, 500, 200, 100, and 10 samples/second with a sampling rate of 500 samples/second used for this work.

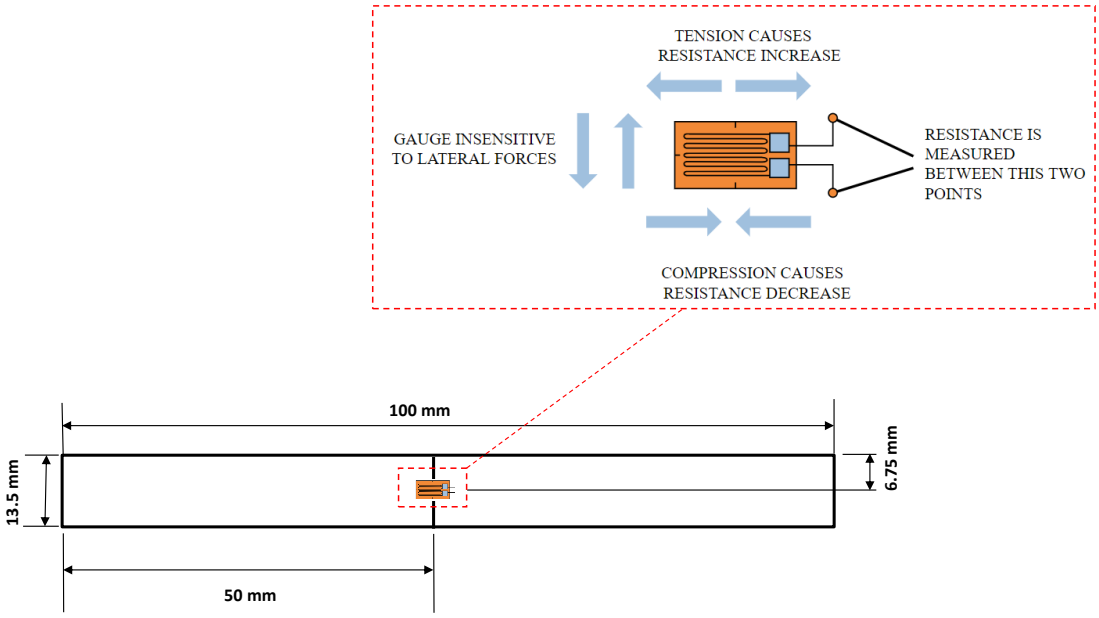

Figure 4: Schematic of half-bridge strain gauge reproduced from [36], and location of the strain gauge on the top surface of the specimen (A second strain gauge was bonded exactly at the same location on the lower surface of the specimen).

2.5 Experimental results

Results from static bending tests show consistent behaviour for all the specimens (Figure 6). A linear elastic relationship between load-carrying capacity and deflection is seen initially. This corresponds to global bending of the laminated specimens in the elastic region. After the yield point is reached, the flexural behaviour of the FML specimen becomes nonlinear corresponding to elastic-plastic bending. This is followed by debonding between the discontinuous aluminium layer and the resin pocket in the doubler joint region accompanied by matrix cracking (Region-1 in Figure 6). As the load increases the delamination grows between the discontinuous aluminium layer and the middle layer of GFRP (Region-2 in Figure 6). Finally, the delamination reaches the edge of the specimen causing layers to visibly slide past each other (Region-3 in Figure 6). Tests were stopped at this point as further damage in the aluminium and composite layers is out of the scope of this study.

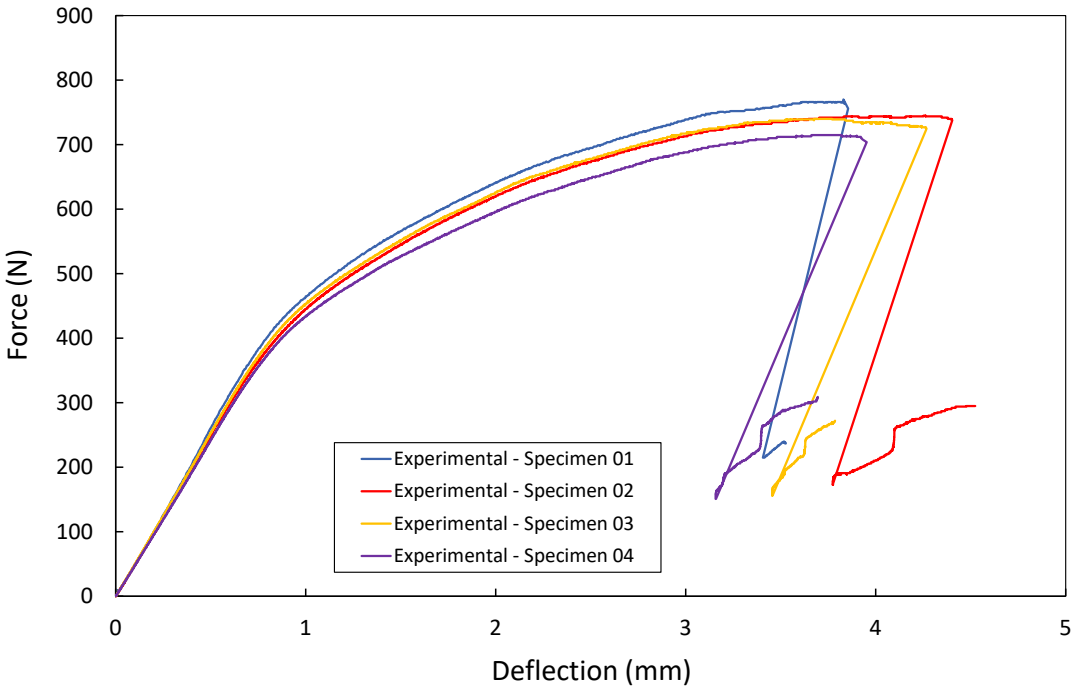

(a)

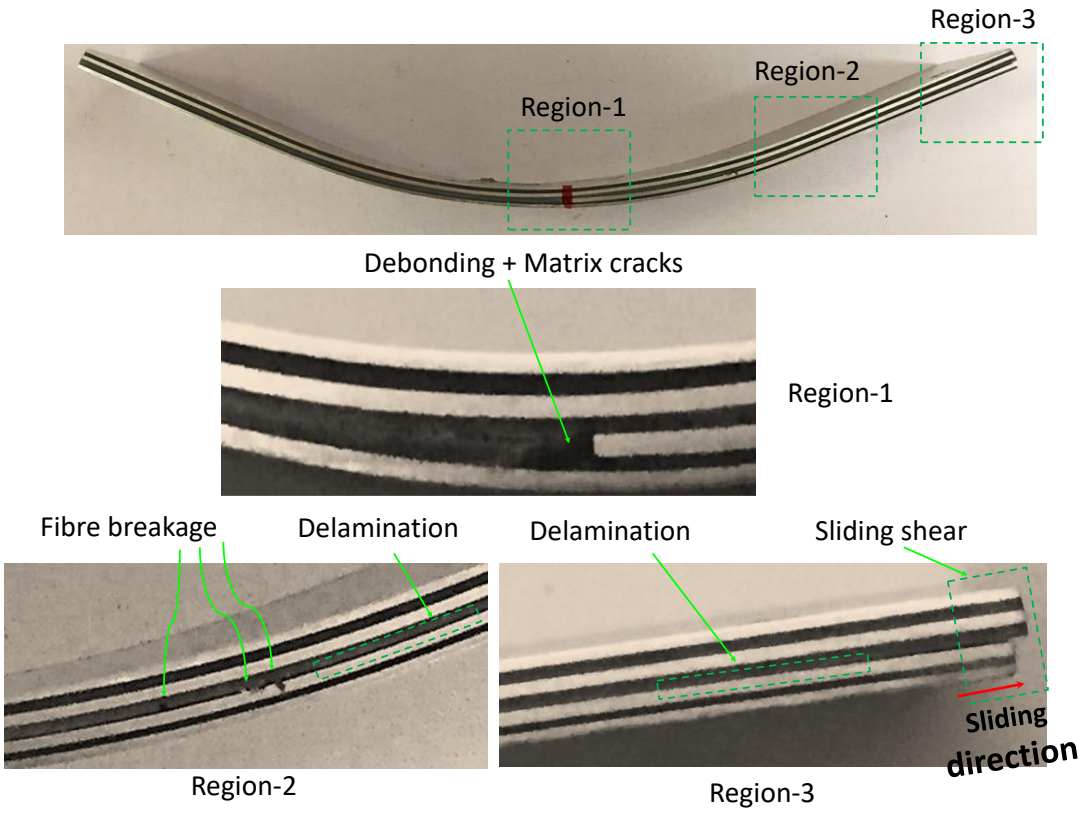

(b)

Figure 6: (a) Experimental force versus deflection curves for doubler specimens, and (b) damage mechanisms for doubler specimen under flexural loads. (For interpretation of the references to colours in this figure, the reader is referred to the web version of this article).

Delamination growth and shear failure occur only in the right-hand (thicker) side of the specimen as shown in Figure 7. This is a result of the stress concentration around the end of the discontinuous aluminium layer close to the joint, which leads to the initiation of a delamination which starts to propagate at the interface of the discontinuous aluminium layer and the GFRP layer above it.

(a) (b) (c)

Figure 7: Delamination propagation and sliding shear failure in the right thick side of doubler specimen 3, at deflection (a) $\delta = 2$ mm, (b) $\delta = 3.5$ mm, (c) $\delta = 3.8$ mm.

No delamination growth or damage was observed in the left-hand (thinner) side of the specimen at any point during the test as shown in Figure 8. This is due to the asymmetry of the specimen with the load distributing more towards the thicker side of the specimen. The toughened resin pocket in the doubler joint also acts to prevent the delamination from propagating leftward through the joint after debonding, favouring growth in the other direction instead.

(a) (b) (c)

Figure 8: Bending deformation showing no delamination in the left thin side of doubler specimen 3, at deflection (a) $\delta = 2$ mm, (b) $\delta = 3.5$ mm, (c) $\delta = 3.8$ mm.

3. Numerical Analysis

3.1 Modified cohesive zone model

For composite structures where the interface is subjected to through-thickness compression stresses $(\sigma_{\mathrm{I}} \leq 0)$, the damage process at the cohesive interface is mostly a pure Mode II problem [26,27]. The constitutive law for an interface in this case is modified by including friction following **Zou and Lee** [39] and hence enhanced traction or shear stress $\acute{\sigma_{\mathrm{II}}}$ can be expressed by:

$$\acute{\sigma_{\mathrm{II}}} = (1-D)\cdot k_{\mathrm{II}}\cdot \delta_{\mathrm{II}} + \mu \cdot k_{\mathrm{I}} \cdot \delta_{\mathrm{I}}, \quad (1)$$

where δ_{I} and δ_{II} are the relative displacement or separation components for modes I and II respectively, k_{I} and k_{II} are the respective penalty stiffnesses, as $\sigma_{\mathrm{I}} = k_{\mathrm{I}} \cdot \delta_{\mathrm{I}}$ then for $\sigma_{\mathrm{I}} = 0$ we will get the baseline CZM without friction and/or shear enhancement effects and for $\sigma_{\mathrm{I}} < 0$ we will get the modified CZM including friction and shear enhancement effects, μ is a friction coefficient and D is a scalar damage variable, usually used to describe three states of failure. For the undamaged interface state, the damage parameter is equal to zero, when the interface is fully fractured (failed) the damage parameter is equal to one. The third state, known as the damaged state, has a damage parameter $0 < D < 1$. The damage variable is determined based on strain energy release rate and given based on power law relation by the following softening expression [40]:

$$D = \left(\frac{G_{\mathrm{I}}}{G_{\mathrm{Ic}}}\right)^{\alpha} + \left(\frac{G_{\mathrm{II}}}{G_{\mathrm{IIc}}}\right)^{\alpha}, \quad (2)$$

where G_{I} and G_{II} are the strain energy release rates for modes I and II respectively, G_{Ic} and G_{IIc} are the experimentally derived critical strain energy release rates (fracture energies) and α is a power law parameter which is given the value of a half according to a best fit for mixed mode delamination data from the literature [41].

A cohesive zone model was developed to consider the enhancing effect of through-thickness compression on mode-II (in-plane shear) fracture. The enhanced interfacial shear strength in the damage model is defined by **Hallett *et al.*** [27] using a modified cohesive zone model (CZM) which introduces an

interfacial shear parameter to model the effect of through-thickness compressive stresses. This modified CZM assumes that the mode-I interface stiffness of the cohesive element remains constant, thus avoiding interpenetration of the laminate interfaces such that the damage has no effect on mode-I behaviour. The effective critical strain energy release rate in mode-II is then given by:

$$G_{\mathrm{IIc}}^{'} = \left(\frac{\sigma_{\mathrm{II}}{}_{\mathrm{max}}^{'}}{\sigma_{\mathrm{II}_{\mathrm{max}}}}\right)^{2} \cdot G_{\mathrm{IIc}} \,, \tag{3}$$

where $\sigma_{\mathrm{II}}{}_{\mathrm{max}}^{'}$ is the enhanced mode-II cohesive strength and $\sigma_{\mathrm{II}_{\mathrm{max}}}$ is the pure mode-II strength in the absence of through-thickness stresses. This equation has been modified here to include both friction and enhanced shear strength (F-S/CZM). Furthermore, a novel mode-II constitutive behaviour model based on the trapezoidal CZM developed by the authors [40] is utilised instead of the conventional bilinear CZM. This was found to be more suitable for simulating the elastic-plastic behaviour of toughened adhesive interfaces for composite structures with a detailed discussion on this reported in [40]. From the conventional traction-separation law, the relationship between the maximum value of traction or stress and the separation or displacement can be described by:

$$\sigma_{\mathrm{II}_{\mathrm{max}}} = k_{\mathrm{II}} \cdot \delta_1 \,. \tag{4}$$

Therefore, a similar relationship has been used for the revised shear strength $\sigma_{\mathrm{II}}{}_{\mathrm{max}}^{'}$ with enhanced separation $\delta_1^{'}$:

$$\sigma_{\mathrm{II}}{}_{\mathrm{max}}^{'} = k_{\mathrm{II}} \cdot \delta_1^{'} \,. \tag{5}$$

From eq. (5) we can derive the value of enhanced separation $\delta_1^{'}$ as:

$$\delta_1^{'} = \frac{\sigma_{\mathrm{II}}{}_{\mathrm{max}}^{'}}{k_{\mathrm{II}}}. \tag{6}$$

Then, using a trigonometric function to describe the trapezoidal relationship (Figure 9) the enhanced shear strength $\sigma_{\mathrm{II}}{}_{\mathrm{max}}^{'}$ can be derived as a function of the conventional shear strength $\sigma_{\mathrm{II}_{\mathrm{max}}}$ as:

$$\sigma_{\mathrm{II}}{}_{\mathrm{max}}^{'} = \sigma_{\mathrm{II}_{\mathrm{max}}} + k_{\mathrm{II}} \cdot \left(\delta_1^{'} - \delta_1\right) \,. \tag{7}$$

Hence, as demonstrated by the finite element analysis implemented by **Hallett *et al.*** [27] the application of a bending load which results in combined through-thickness compression or tension and shear acting on the cohesive interlaminar layers, *i.e.* mixed mode rather than the desired shear mode, can be represented as a pure mode-II shear failure, through the introduction of an enhanced shear parameter η in the mode-II shear stress relation as:

$$\sigma_{\mathrm{II}_{\max}}^{'} = \sigma_{\mathrm{II}_{\max}} - \eta \cdot \sigma_{\mathrm{I}} \quad \text{when } \sigma_{\mathrm{I}} < 0. \tag{8}$$

In this study we also introduce the effect of friction (as recommended by many researchers for composites [28-33] but as yet not used in FMLs), as it has been proven that including both friction and enhanced shear strength gives more accurate results for the simulation of the effect of through-thickness compression on mode-II shear failure. This has been achieved using a further modification to the cohesive zone model (F-S/CZM) coupling both friction and enhanced shear strength and implemented by combining eqs. (1) and (8):

$$\sigma_{\mathrm{II}_{\max}}^{'} = \sigma_{\mathrm{II}_{\max}} - \mu \cdot \sigma_{\mathrm{I}} - \eta \cdot \sigma_{\mathrm{I}} \quad \text{when } \sigma_{\mathrm{I}} < 0. \tag{9}$$

Separation or displacement in the elastic region can be calculated based on the new F-S/CZM model by dividing eq. (9) by the mode-II stiffness k_{II} after substituting the normal and shear stresses as functions of (k) and (δ):

$$\delta_1^{'} = \delta_1 - \mu \cdot \frac{k_{\mathrm{I}}}{k_{\mathrm{II}}} \cdot \delta_{\mathrm{I}} - \eta \cdot \frac{k_{\mathrm{I}}}{k_{\mathrm{II}}} \cdot \delta_{\mathrm{I}} \quad , \tag{10}$$

where δ_1 is the maximum separation based on the pure shear strength $\sigma_{\mathrm{II}_{\max}}$ and $\delta_1^{'}$ is the maximum separation for the enhanced shear strength $\sigma_{\mathrm{II}_{\max}}^{'}$ (Figure 9).

Based on the trapezoidal CZM developed by **Tvergaard and Hutchinson** [42] a relationship can be built based on the shape parameter β:

$$\delta_2^{'} = \delta_1^{'} + \left(\acute{W} \cdot \beta\right) \quad , \tag{11}$$

$$\delta_3^{'} = \delta_1^{'} + \acute{W} \quad , \tag{12}$$

where $\delta_2^{'}$ and $\delta_3^{'}$ are the separations based on the enhanced mode-II strengths for both constant stress and softening regions respectively (see Figure 9), while $\acute{W}$ is a variable which is derived based on the trapezoidal law and for which the

explicit expressions are listed in Appendix-A. The final definition of $\acute{W}$ is given by:

$$\acute{W} = \frac{G_{\mathrm{IIc}}^{\prime} - \frac{\left(\sigma_{\mathrm{II}}{}_{\mathrm{max}}^{\prime}\right)^2}{2 \cdot k_{\mathrm{II}}}}{\sigma_{\mathrm{II}}{}_{\mathrm{max}}^{\prime} \cdot \left(\frac{\beta+1}{2}\right)}. \tag{13}$$

The total fracture energy for the (F-S/CZM) is given by the total area under the modified traction-separation curve, and can be calculated simply by dividing the trapezoid into three regular areas (Figure 9):

$$G_{\mathrm{IIc}}^{\prime} = A_1^{\prime} + A_2^{\prime} + A_3^{\prime}\ , \tag{14}$$

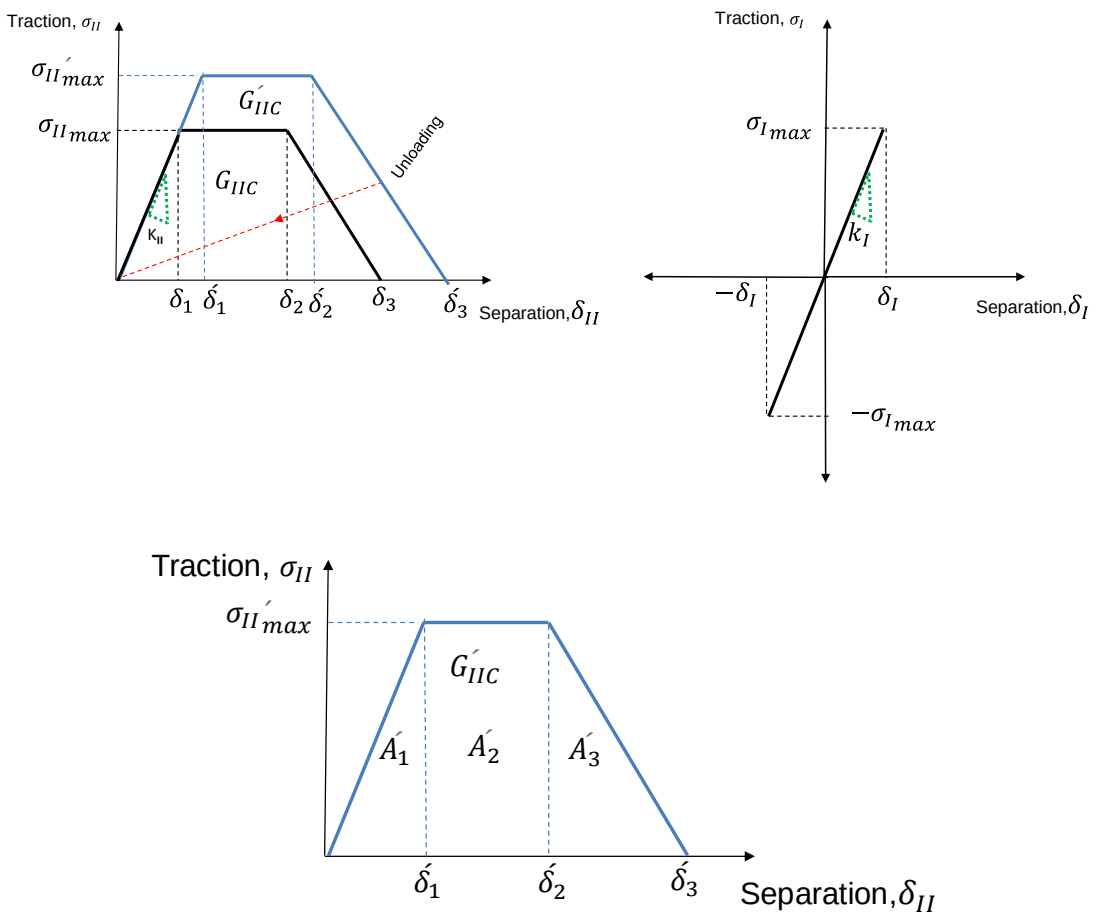

Figure 9. Constitutive behaviour of trapezoidal based CZM reported by the author in [40] and with enhanced mode-II properties new model (F-S/CZM).

where $A_1^{\prime}, A_2^{\prime}, A_3^{\prime}$ represent the strain energy release rate in the elastic, constant stress and softening regions:

$$A_1^{'} = \frac{1}{2} \cdot \delta_1^{'} \cdot \sigma_{\mathrm{II}}{}_{\max}^{'} \quad , \tag{15}$$

$$A_2^{'} = \sigma_{\mathrm{II}}{}_{\max}^{'} \cdot \left(\delta_2^{'} - \delta_1^{'}\right) \quad , \tag{16}$$

$$A_3^{'} = \frac{1}{2} \cdot \sigma_{\mathrm{II}}{}_{\max}^{'} \cdot \left(\delta_3^{'} - \delta_2^{'}\right) \ . \tag{17}$$

To calculate these, we first need to find the maximum enhanced shear stress and separation within each area. This can be done by solving eq. (10) to obtain $\delta_1^{'}$ using the normal separation δ_{I} which can be calculated based on the conventional traction-separation relationship:

$$\delta_{\mathrm{I}} = \sigma_{\mathrm{I}} / \, k_{\mathrm{I}} \ , \tag{18}$$

where σ_{I} is the through-thickness compressive stress for mode-I and k_{I} is the mode-I cohesive stiffness. After calculating $\delta_1^{'}$ we can substitute this value into eq. (7) to find $\sigma_{\mathrm{II}}{}_{\max}^{'}$. Then, we can calculate modified separations $\delta_2^{'}$ and $\delta_3^{'}$ using similar approach to that in eq. (10):

$$\delta_2^{'} = \delta_2 - \mu \cdot \frac{k_{\mathrm{I}}}{k_{\mathrm{II}}} \cdot \delta_{\mathrm{I}} - \eta \cdot \frac{k_{\mathrm{I}}}{k_{\mathrm{II}}} \cdot \delta_{\mathrm{I}} \quad , \tag{19}$$

$$\delta_3^{'} = \delta_3 - \mu \cdot \frac{k_{\mathrm{I}}}{k_{\mathrm{II}}} \cdot \delta_{\mathrm{I}} - \eta \cdot \frac{k_{\mathrm{I}}}{k_{\mathrm{II}}} \cdot \delta_{\mathrm{I}} \quad . \tag{20}$$

Finally, we can substitute these separation values into eq. (14) to find the modified total fracture energy $G_{\mathrm{IIc}}^{'}$ which can also be calculated from eq. (3).

3.2 Simplified finite element model

A 2D simplified FE model was first generated to validate the new cohesive zone model (F-S/CZM) including through-thickness compression stresses (Figure 10). The geometry consisted of one layer of aluminium and two layers of GFRP, with cohesive elements inserted at the aluminium/GFRP interface. Symmetry was used to reduce computational time by modelling half the 4-point bending test. Two rollers were used, one for applying load and the other to simulate the support. Simply-supported boundary conditions were introduced along the left-hand edge to represent the half-symmetry. Fixed boundary conditions were applied to the support roller, while for load roller y-direction

displacements were prescribed whilst the x and z directions were fixed. The right-hand edge of the model remained free. The aluminium layer was 0.4 mm thick and the GFRP plies were 0.127 mm thick each. Each layer was meshed using 4-noded bilinear plane stress CPS4R elements. The interfaces between each layer were meshed using COH2D4 cohesive elements. The laminate was then assembled, and material properties were assigned accordingly based on a comprehensive literature review of the mechanical properties for Glare material constituents (Tables 1 to 4).

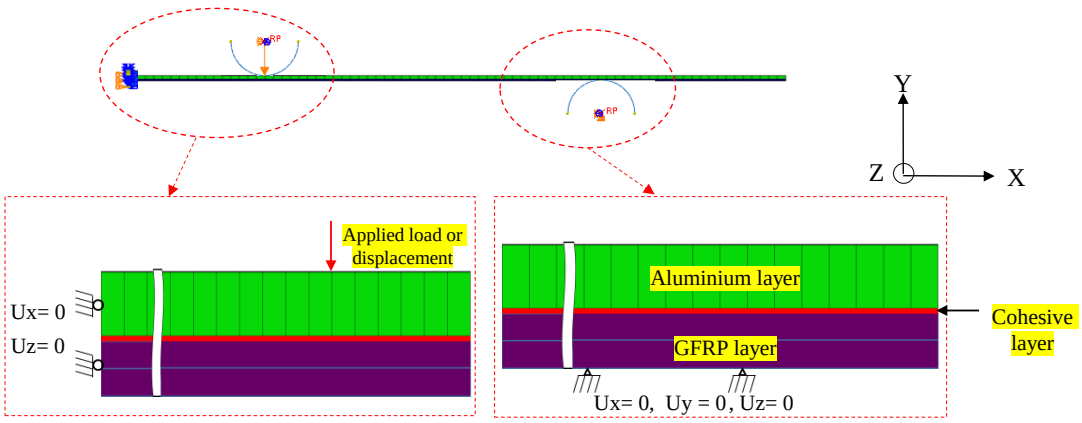

Figure 10: Half-symmetry 2D simplified FE model for 4-point bending analysis.

Table 1: Mechanical properties for aluminium alloy 2024-T3 [37].

Property	Value	Units
Young's modulus	72.4	GPa
Stress at 4.7% strain	420	MPa
Shear modulus	27.6	GPa
Poisson's ratio	0.33	-
Mass density	2780	$kg \cdot m^{-3}$

Table 2. Plasticity data for aluminium 2024-T3 [43]

Yield stress (MPa)	300	320	340	355	375	390	410	430	450	470	484
Plastic strain (%)	0.00	0.016	0.047	0.119	0.449	1.036	2.130	3.439	5.133	8.00	14.71

Table 3: Mechanical properties for S2-glass/FM94 prepreg material [44]

Property	Value	Units
Young's modulus, fibre direction, E_{11}	50.0	GPa
Young's modulus, transverse direction, E_{22}	9.0	GPa
Poisson's ratio, ν_{12}	0.33	-
Poisson's ratio, ν_{23}	0.04	-
In-plane shear modulus, G_{12}	3.5	GPa
Transverse shear modulus, G_{23}	3.0	GPa
Fibre-direction tensile strength, X_{T}	2000	MPa
Fibre-direction compressive strength, X_{C}	550	MPa
Transverse tensile strength, Y_{T}	43	MPa
Transverse compressive strength, Y_{C}	90	MPa
In-plane shear strength, S_{12}	93	MPa
Transverse shear strength, S_{23}	50	MPa
Critical SERR*, fibre direction, $G_{c,X}$	12.0	kJ·m^{-2}
Critical SERR*, transverse direction, $G_{c,Y}$	1.0	kJ·m^{-2}
Mass density, ρ [45]	2000	kg·m^{-3}

*Strain Energy Release Rate.

Table 4: Cohesive zone properties for metal/GFRP interfaces.

G_{Ic} (kJ·m^{-2}) [46]	G_{IIc} (kJ·m^{-2}) [46]	$\sigma_{\mathrm{I}_{\max}}$ (MPa) [46]	$\sigma_{\mathrm{II}_{\max}}$ (MPa) [46]	k_{I} (N·mm^{-3})	k_{II} (N·mm^{-3})	ρ (g/cm^3)
0.45	1.0	40	40	2.189×10^5	0.823×10^5	1.5

Two main coefficients are used to represent the effects of the through-thickness compression stresses. First a **friction coefficient** μ, based on the phenomenological delamination criterion proposed by [38] based on a modified Mohr–Coulomb friction mechanism and second an **enhanced shear factor** η which was found in [26] to give an accurate prediction for delamination and shear failure in GFRP laminates. As the latter mainly depends on the intelaminar shear strength (ILSS) of the laminate, which was found by **Bellini** [21] to be similar for both GLARE and GFRP it is anticipated that this factor will also be important in the failure of Glare.

In the work of **Hallett *et al.*** [26], an **enhanced shear factor** η=0.65 was found to give an accurate prediction for delamination and shear failure in GFRP laminates, and it has therefore been used in this study in the absence of experimental data for Glare laminates. The authors also considered delamination and shear failure at the aluminium/GFRP interfaces since this is the predominant failure mode in Glare laminates under bending loads. Here failure is mostly due to the increasing shear strain in the GFRP plies which transfers from the metal layers due to bridging stresses [37] as the aluminium layers are plasticly deformed. This is seen in the work of **Liu *et al.*** [3] (as mentioned earlier in Section 1), who studied curved GLARE laminates under bending and found through inspection of SEM images of the fiber/metal interface for three different ply angles that as the bending stress increased the metal layer began to yield, while the fiber layer continued to elastically deform. As the bending stress continued to increase, a large amount of fiber breakage occurred. When the bearing limit was reached, interlaminar delamination failure occurred in the metal/fiber layer. Following this conclusion in the current study we considered the failure in Glare laminate is mainly as a consequence of the GFRP behaviour and therefore the same value of enhanced shear coefficient η of GFRP/GFRP interfaces is considered for the GFRP/metal interfaces.

Furthermore for thin Glare laminates and according to **Liu** [9] who considered that composite layer and the metal layer were laid in the same angle, we assumed that the fracture angle of GFRP plies is approximately equal to the fracture angle of adjacent aluminium/GFRP interfaces, and based on a modified Mohr–Coulomb friction formula which considers **friction coefficient** μ is a function of the fracture angle only, therefore we assumed friction coefficient for GFRP is equal to the friction coefficient for aluminium/GFRP interfaces in Glare laminate.

The value of **friction coefficient** μ=0.31 also used in this work was introduced by **Xiao *et al.*** [38], who used experimental results from S2-glass/epoxy composite laminates subject to combined interfacial shear through-thickness compressive stresses. This value is superimposed on initial friction and increases nonlinearly. It is introduced at the beginning of cohesive softening (damage initiation). This new phenomen-ological delamination criterion is proposed by the authors to enable consideration of the effects of through-

thickness compression based on a modified Mohr–Coulomb friction mechanism. Their experimental results show that through-thickness compression increases interlaminar shear (ILS) strength nonlinearly, requiring a nonlinear friction function. The proposed delamination criterion considers the full extent of the ILS increase observed in the available experiments.

The model is implemented in the Abaqus/Explicit solver with a VUMAT user-defined subroutine for cohesive materials including the new cohesive zone model (F-S/CZM). Figure 11 shows how the interfacial shear strength enhancement and friction affect the shear traction-separation curve of the cohesive zone model under through-thickness compression for this simplified model. The following observations can be made by comparing the curves. Adding both shear strength and friction parameters ($\eta = 0.65$, $\mu = 0.31$) causes a significant increase in the shear stress on the interface and therefore the fracture energy $G_{\mathrm{IIc}}^{'}$ which increases to almost double the original fracture energy G_{IIc}. Using shear strength enhancement only ($\eta = 0.65$, $\mu = 0$) leads to an increase fracture energy of about 60% while using the friction coefficient on its own ($\eta = 0$, $\mu = 0.31$) increases the fracture energy by only 24 %.

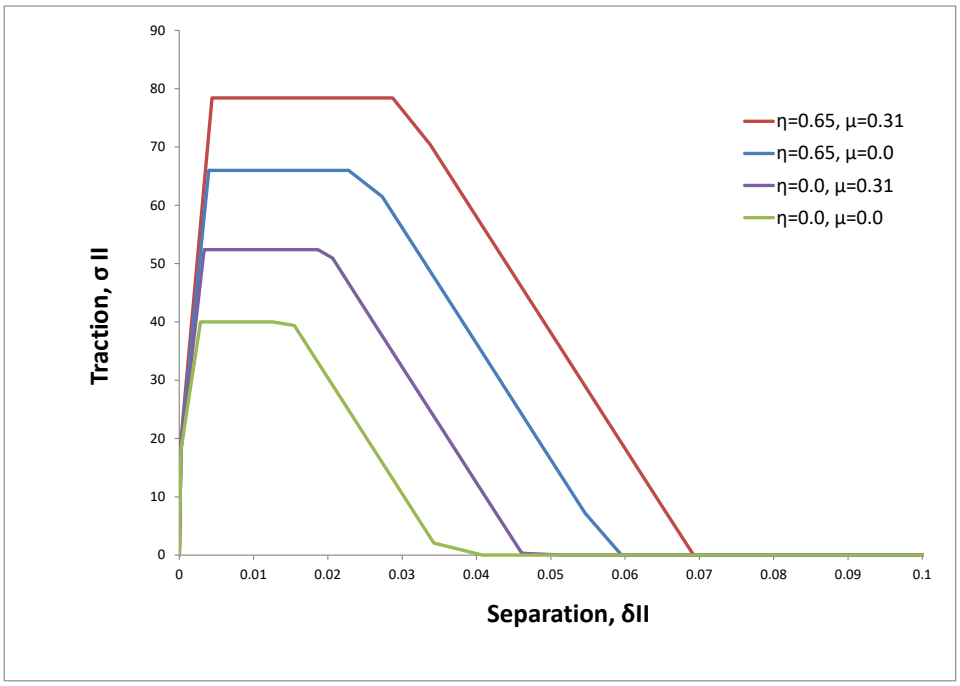

Figure 11: Traction-separation relationships for the cohesive interface for the simplified model including the effect of shear strength enhancement and friction on the interlaminar shear. (For interpretation of the references to colours in this figure, the reader is referred to the web version of this article).

3.3 Doubler specimen finite element model

A full FE model was then developed to simulate the quasi-static 4-point bending test of the doubler specimens, again in Abaqus/Explicit. The model, illustrated in Figure 12, consists of a 2D cross-section of the specimen with two rigid roller supports and two rigid loading rollers corresponding to the experimental set-up. The support rollers were fixed in all directions. The loading rollers were subjected to a uniform motion in the y direction and fixed in both the x and z directions. To ensure reasonable computational times, the total time was set to 0.2 s with the time step manually adjusted using mass scaling until the resulting artificial strain energy (ALLAE) was less than 1% of the total internal energy (ALLIE) [47]. This ensured the model would be insensitive to the rate of loading and thus representative of a quasi-static loading scheme. The constituent materials were modelled using the 2D plane stress element CPS4R while the 2D cohesive element COH2D4 was used to model the interlaminar layer between the metal and the fibre. The full untabbed 100 mm length of the specimen was modelled. Interface elements were placed along the delamination site of the gauge region (Figure 13), with an interface thickness of 0.01 mm. In order to ensure suitable element sizes, especially in the area of the interfaces and through the doubler joint, sensitivity studies were performed and a mesh size with in-plane element lengths of 1 mm for all elements was chosen. The rollers were modelled using analytical rigid surfaces in order to reduce computational time. A penalty-based surface-to-surface contact with a coefficient of friction of 0.05 was introduced [48]. Delamination at the aluminium/GFRP interfaces was modelled using cohesive elements. Damage in the composite layers was monitored using the built-in 2D Hashin damage criterion which includes compressive and tensile failure along the fibre direction and in the in-plane transverse direction (for simplicity the former is referred to as ‘fibre failure’ and the latter as ‘matrix failure’). Plastic deformation in the aluminium was also modelled. To minimise hourglassing when using the reduced-integration CPS4R element, 8 elements were introduced through the thickness of each ply [47]. A traction-separation constitutive damage model was used for the resin pocket region including the doubler joint. The material properties for the metal layers and unidirectional composite laminates are given in Tables 1, 2 and 3.

The fracture process resulting from delamination at the metal/GFRP interfaces is micro-mechanically different from the fracture process observed between the same metal and the same resin in the absence of fibres, since the presence of fibres precludes the development of a local plastic zone within the toughened epoxy material [49]. As a result, much higher fracture energies are expected within the resin pocket formed around doubler feature in the laminate investigated here. Indeed, **Katnam *et al.*** [50] obtained the cohesive properties shown in Table 4 for fracture in a similar material system, but along a 100 μm thick unreinforced resin layer. The properties in Tables 5 and 6 were therefore assumed for the resin pockets and the interfaces formed around resin pockets, respectively.

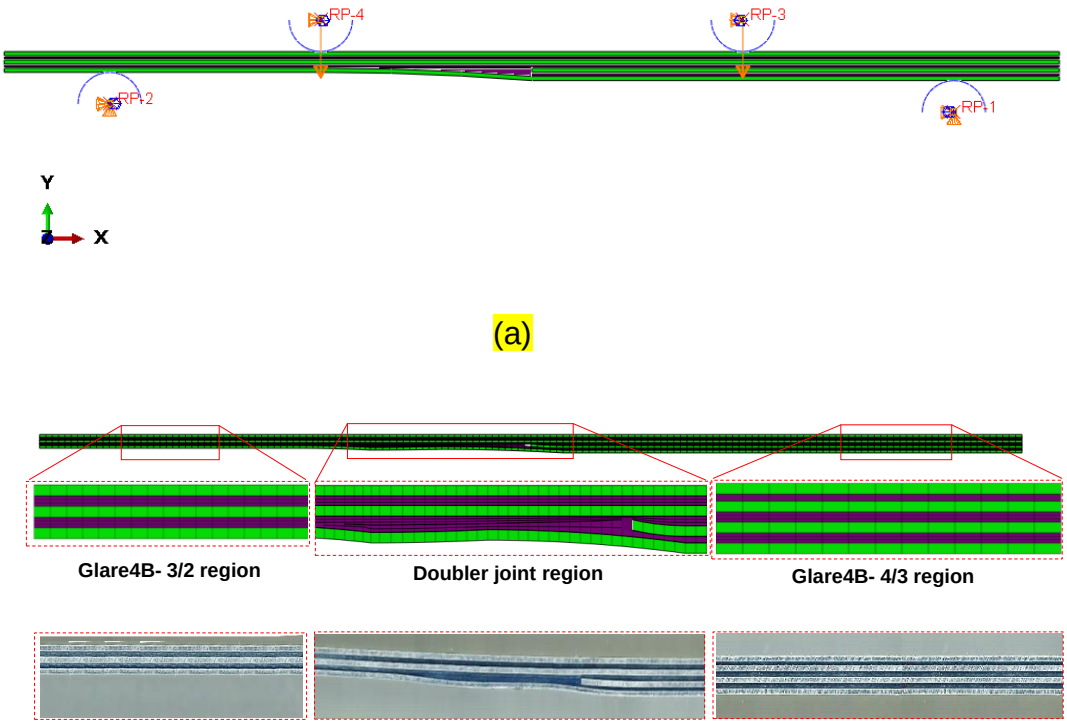

Figure 12: (a) Applied load and boundary conditions for the 4-point bending 2D FE model, (b) Finite element mesh of the doubler specimen (top) based on optical scans of real specimens (bottom) (images resized for clarity, not to scale).

Table 5: Mechanical properties for the FM94 resin [51].

Property	Value	Units
Young's modulus	2.19	GPa
Poisson's ratio	0.33	-
Mass density [51, 52]	1280	kg·m^{-3}

Table 6: Cohesive zone properties for bulk resin/metal interfaces.

G_{Ic} (kJ·m^{-2}) [50]	G_{IIc} (kJ·m^{-2}) [50]	$\sigma_{\mathrm{I}_{\max}}$ (MPa) [41]	$\sigma_{\mathrm{II}_{\max}}$ (MPa) [41]	k_{I} (N·mm^{-3})	k_{II} (N·mm^{-3})
2.0	4.0	50	50	2.189×10^{5}	0.823×10^{5}

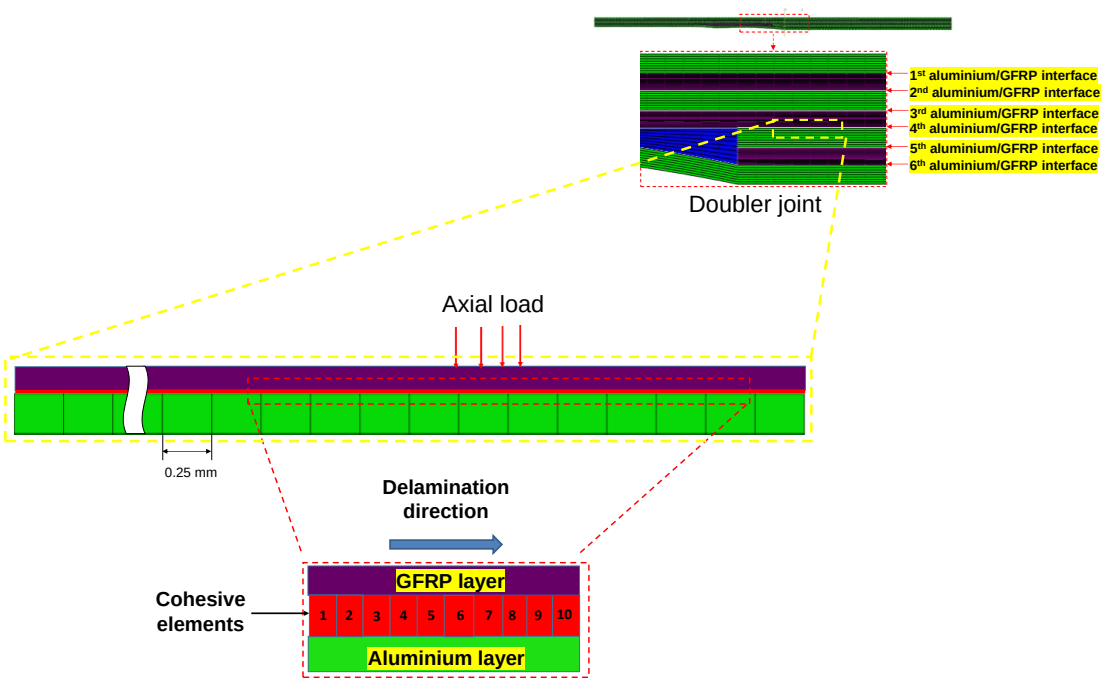

Figure 13: Mesh design for doubler specimen including locations of cohesive elements layers which represent (aluminium/GFRP) interfaces and location of a sample set of 10 cohesive elements. (images resized for clarity, not to scale).

The results for the delamination at the 4th aluminium/GFRP interfaces are presented in terms of traction-separation relationships at the 4th aluminium/GFRP interface (Figure 13) since the other interfacial layers do not show noticeable delamination.

Figure 14 shows the effect of the interfacial shear strength enhancement and friction on the shear traction-separation curves of a set of 10 cohesive elements which represent part of the aluminium/GFRP interface between the discontinuous aluminium layer and the middle GFRP layer. Figure 14-a presents the results obtained adding both shear strength and friction parameters ($\eta = 0.65$, $\mu = 0.31$) causing a significant increase in the shear stress on the interface, and therefore the fracture energy $G_{\mathrm{IIc}}^{'}$ is nearly twice the original fracture energy G_{IIc}. Figure 14-b shows that adding only shear strength enhancement ($\eta = 0.65$, $\mu = 0.0$) without friction leads to an increase in fracture energy of about 60%, while adding only the friction coefficient ($\eta = 0$, $\mu = 0.31$) increases the energy by about 24 % (Figure 14-c). Finally, Figure 14-d shows the case for zero friction or shear enhanced parameters ($\eta = 0$, $\mu = 0$).

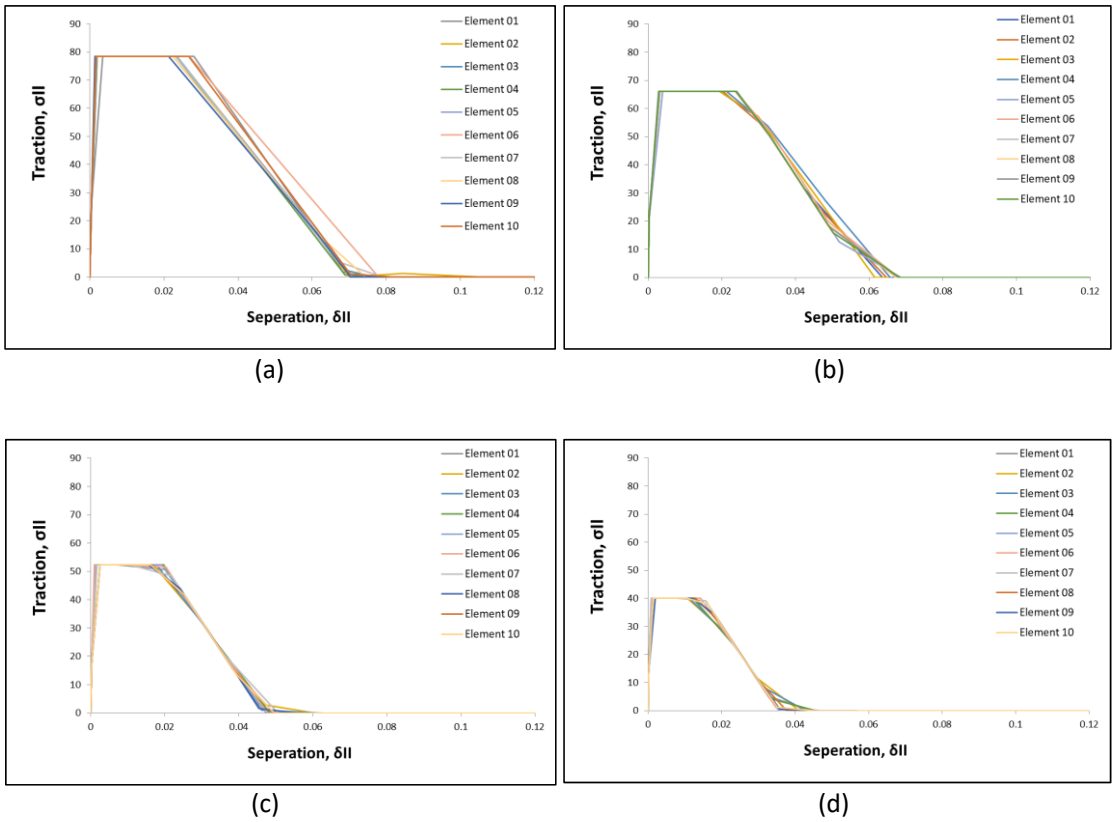

Figure 14: Traction-separation curves for a set of 10 cohesive elements in the doubler specimen model including effect of the shear strength enhancement and friction parameters on the interlaminar shear; (a) $\eta = 0.65$, $\mu = 0.31$, (b) $\eta = 0.65$, $\mu = 0$, (c) $\eta = 0$, $\mu = 0.31$, and (d) $\eta = 0$, $\mu = 0$.

Since the enhancement of the apparent in mode-II fracture energy is highly dependent on the assumed enhanced parameters, comparisons with

experimental results are required to validate the choice of these constants. The force-deflection curves obtained from the static 4-point bending tests are therefore compared with those from the FE model in Figure 15. It can be seen that the original trapezoidal CZM model results in severe underestimations of the damage initiation and propagation behaviours, but with a good prediction of the elastic response of the specimens. This is a direct consequence of using a CZM which neglects the effects of through-thickness compression on the shear strength and friction. On the other hand, the predicted results using the cohesive zone model proposed here (F-S/CZM) are in much better agreement with the experimental data. Whilst the FE model results in an overestimation of the stiffness in the elastic-plastic bending region compared to the experimental results, there is excellent agreement in terms of the predominant damage behaviours (delamination and shear) and maximum bending force. It should be noted that the nonlinear behaviour of the model is a combination of plasticity in aluminium layers (Table 2), Hashin damage in GFRP layers [53], and the ductile damage in resin pockets [54], with material data mostly taken from the literature. In addition, the model neglects thermal residual stresses introduced during autoclave cure, since it is a 2D plane strain representation of the doubler specimens. The combination of all these factors is believed to be responsible for the stiffness overestimation in the elastic-plastic bending regime.

In this study a value for the enhanced shear coefficient η=0.65 and friction coefficient μ=0.31 are shown to give an excellent prediction of the bending behaviour of Glare laminates using a modified CZM and this is confirmed by the numerical model results in Figures 14 and 15, where they are compared with experimental results using the revised critical strain energy release rate in mode-II $(\acute{G}_{\mathrm{IIc}})$ considering both enhanced shear and friction coefficients. Removing either one or both of these coefficients using a baseline critical strain energy release rate (G_{IIc}) causes significant underestimation of overall damage behaviour and bending failure. These results are aligned with those in [20] where it was found that for Glare laminates under through-thickness compression stresses a significant amount of energy is absorbed by friction, intralaminar damage, plastic deformation of the aluminium, debonding and delamination.

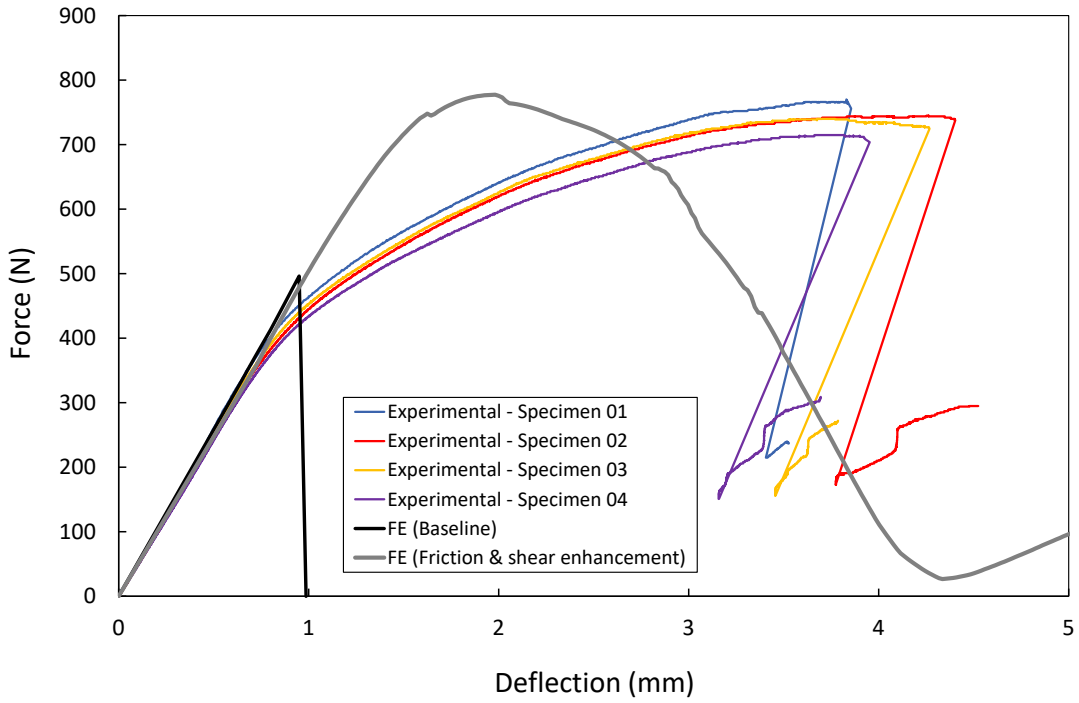

Figure 15: Static bending load-deflection curves for doubler specimens, comparison between original CZM FE model results [40] (without friction and shear enhancement), new (F-S/CZM) FE model results (with friction and shear enhancement) and experimental results. (For interpretation of the references to colour in this figure legend, the reader is referred to the web version of this article).

4. Conclusions

A novel cohesive zone model was developed for Glare® fibre-metal laminates which takes into account the enhancement of apparent interfacial shear properties (strength and strain energy release rates) as well as frictional effects in the presence of compressive through-thickness stresses. The model is implemented in the Abaqus/Explicit software via the user subroutine VUMAT. The modified trapezoidal traction-separation law is validated against a simplified 2D FE model and then against experimental results from four-point bending tests on a series of Glare® specimens containing doubler joints. Delamination and shear failure of aluminium / GFRP interfaces were investigated. Stress concentrations due to the existence of discontinuous aluminium layers allow damage to initiate at relatively small loads, followed by debonding between the resin pocket and the discontinuous aluminium layer. This interlaminar damage behaviour is efficiently predicted by the proposed model. The thinner side of the doubler specimen (Glare 4B-3/2 laminate) shows higher levels of deformation compared with the thicker part (Glare 4B-4/3

laminate), which is a result of the asymmetry in the doubler specimen. As loading progresses delamination and shear failure are observed in the thicker side of the specimen, while in the thin side no delamination is seen. This is because the toughened resin pocket in the doubler joint prevents delamination propagation through the joint after initial debonding at the discontinuity, leading to delamination growth in the opposite direction between the discontinuous aluminium layer and the middle GFRP layers. This behaviour is observed both in experiments and FE models.

5. Acknowledgements

The authors would like to thank the Iraqi Ministry of higher education and scientific research and the University of Babylon for supporting this research. Also the technical staff of the Cardiff School of Engineering for their kind assistance with the testing programme.

References

[1] A.D. Vlot and J.W. Gunnink, Fibre Metal Laminates - An Introduction. 2001, London: Kluwer Academic publishers.

[2] H. Berends, E. van Burg, E.M. van Raaij, Contacts and Contracts: Cross-Level Network Dynamics in the Development of an Aircraft Material. Organization Science, 2011. 22(4): p. 940–960.

[3] C. Liu, D. Du, H. Li, Y. Hu, Y. Xu, J. Tian, G. Tao, J. Tao, Interlaminar failure behaviour of GLARE laminates under short-beam three-point bending load, Composite Part B: Engineering, vol.97, pp.361-367, 2016.

[4] Y. Xu, Research on bending properties and failure mechanisms of GLARE laminates, Master thesis, Nanjing University of Aeronautics and Astronautics, Nanjing, China, 2017.

[5] J. Ye, C. Chu, H. Cai et al., A multi-scale modelling scheme for damage analysis of composite structures based on the high-fidelity generalized method of cells, Composite Structures, vol. 206, pp.42-53,2018.

[6] Y. Xu, Preparation and properties of Ti/CF/PMR polyimide super hybrid laminates, PhD thesis, Nanjing University of Aeronautics, Nanjing, China, 2017.

[7] H. Aghamohammadi, S.N.H. Abbandanak, R. Eslami-Farsani, and S.M.H. Siadati, Effect of various aluminium surface treatments on the basalt fibre metal laminates interlaminar adhesion, International Journal of Adhesion and Adhesives, vol. 84, pp. 184-193, 2018.

[8] H.L. Schreyer and A. Peffer, Fiber pullout based on a one-dimensional model of decohesion, Mechanics of Materials, vol. 32, no. 12, pp. 821-836, 2000.

[9] C. Liu, Study on interlaminar shear failure behaviour and mechanism of GLARE laminates, Master thesis, Nanjing University of Aeronautics and Astronautics, Nanjing, China, 2017.

[10] C.M. Cepeda-Jimenez, R.C. Alderliesten, O.A. Ruano and F. Carreno, Damage tolerance assessment by bend and shear tests of two multilayer composites: glass fibre reinforced metal

laminate and aluminium roll-bonded laminate, Composite Science and Technology, vol.69, no. 3-4, pp. 343-348, 2009.

[11] P.-C. Yeh, P.-Y. Chang, J.-M. Yang, P.H. Wu, and M.C. Liu, Blunt notch strength of hybrid boron/glass/aluminium fiber metal laminates, Materials Science and Engineering: A, vol. 528, no. 4-5, pp. 2164-2173, 2011.

[12] J.G. Carrillo and W.J. Cantwell, Mechanical properties of a novel fiber–metal laminate based on a polypropylene composite. Mechanics of Materials 2009. 41 p. 828–838.

[13] D. Jung, H. Kim, N. Choi, Aluminum–GFRP hybrid square tube beam reinforced by a thin composite skin layer, Composites: Part A 40 (2009) 1558–1565.

[14] N.A. Husain, C.L. Pang, M.R. Abdullah and M.A. Abu Bakar, Experimental Analysis of Bending and Tensile Behaviour of Aluminium-based Fibre Metal Laminates, in 9th International Conference on Fracture & Strength of Solids. 2013: June 9-13, 2013, Jeju, Korea.

[15] G.R. Rajkumar, M. Krishna, H.N. Narasimhamurthy, Y.C. Keshavamurthy and J.R. Nataraj, Investigation of tensile and bending behaviour of Aluminium based hybrid fibre metal laminates, Procedia materials science, Volume 5, 2014, Pages 60-68.https://doi.org/10.1016/j.mspro.2014.07.242

[16] K. Jin, H. Wang, J. Tao and D. Du, Mechanical analysis and progressive failure prediction for fibre metal laminates using a 3D constitutive model, Composites Part A: Volume 124, September 2019, 105490, https://doi.org/10.1016/j.compositesa.2019.105490

[17] G.S. Dhaliwal and G.M. Newaz, Experimental and numerical investigation of flexural behavior of carbon fiber reinforced aluminum laminates, Journal of Reinforced Plastics and Composites 2016, Vol. 35(12) 945–956, DOI: 10.1177/0731684416632606

[18] M. Mansourinik and F. Taheri-Behrooz, The effect of interface debonding on flexural behaviour of composite sandwich beams, Journal of Sandwich Structures & Materials 2020, Vol. 22(4) 1132–1156. doi.org/10.1177/1099636218781981.

[19] H. Fallahia, F. Taheri-Behrooza and A. Asadi, Nonlinear Mechanical Response of Polymer Matrix Composites: A Review, Polymer Reviews 2020, Vol. 60, No. 1, 42–85. doi.org/10.1080/15583724.2019.1656236.

[20] S. Azhdari, S. Fakhreddini-Najafabadi, F. Taheri-Behrooz, An experimental and numerical investigation on low velocity impact response of GLAREs, Composite Structures 271, 114123, 2021. doi.org/10.1016/j.compstruct.2021.114123.

[21] C. Bellini, Damage analysis of a GLARE laminate subjected to interlaminar shear, Procedia Structural Integrity 25 (2020) 262–267.

[22] L. Gornet, H. Ijaz and D.D.R. Cartie, *Inelastic Interface Damage Modeling with Friction Effects: Application to Z-Pinning Reinforcement in Carbon Fiber Epoxy Matrix Laminates*, Journal of Composite Materials, vol. 44, No. 17/2010

[23] M. Musto and G. Alfano, A fractional rate-dependent cohesive-zone model, Int. J. Numer. Meth. Engng 2015; 103:313–341. DOI: 10.1002/nme.4885

[24] Z. Zou, M. Hameed, Combining interface damage and friction in cohesive interface models using an energy based approach, Composites Part A 112 (2018) 290–298, https://doi.org/10.1016/j.compositesa.2018.06.017

[25] R. Vodiˇcka, E. Kormaníková and F. Kšiˇnan, Interfacial debonds of layered anisotropic materials using a quasi-static interface damage model with Coulomb friction, Int. J. Fract. (2018) 211:163–182, https://doi.org/10.1007/s10704-018-0281-z

[26] X. Li, S.R. Hallett, M.R. Wisnom, Predicting the effect of through-thickness compressive stress on delamination using interface elements, Composites: Part A 39 (2008) 218–230, doi: 10.1016/j.compositesa.2007.11.005

[27] K.W. Gan, S.R. Hallett and M.R. Wisnom, Measurement and modelling of interlaminar shear strength enhancement under moderate through-thickness compression. Composite: Part A, 49,2013. p. 18–25, https://doi.org/10.1016/j.compositesa.2013.02.004

[28] H. Baek, K. Park, Cohesive frictional-contact model for dynamic fracture simulations under compression, International Journal of Solids and Structures 144–145 (2018) 86–99, https://doi.org/10.1016/j.ijsolstr.2018.04.016

[29] Z. Zou, H. Lee, A cohesive zone model taking account of the effect of through-thickness compression, Composites: Part A 98 (2017) 90–98, http://dx.doi.org/10.1016/j.compositesa.2017.03.015

[30] G.R. Ibrahim, A. Albarbar, A new approach to the cohesive zone model that includes thermal effects, Composites Part B 167 (2019) 370–376, https://doi.org/10.1016/j.compositesb.2019.03.003

[31] P.F. Liu, Z.P. Gu and X.Q. Peng, A nonlinear cohesive/friction coupled model for shear induced delamination of adhesive composite joint, Int J Fract (2016) 199:135–156, DOI 10.1007/s10704-016-0100-3

[32] R. Serpieri and G. Alfano, Bond-slip analysis via a thermodynamically consistent interface model combining interlocking, damage and friction, Int. J. Numer. Meth. Engng 2011; 85:164–186, DOI: 10.1002/nme.2961

[33] M.A. Hameed, G.R. Ibrahim and A. Albarbar, Effect of friction and shear strength enhancement on delamination prediction, Journal of Composite Materials 2020, Vol. 54(23) 3329–3342, DOI: 10.1177/0021998320911719

[34] D 7264/D 7264M – 07, Standard Test Method for Flexural Properties of Polymer Matrix Composite Materials, ASTM International, 100 Barr Harbor Drive, PO Box C700, West Conshohocken, PA 19428-2959, United States.

[35] High-Elongation Strain Measurements, Tech Tip TT-605, document Number: 11085 Revision 13-Jul-2015, www.micro-measurements.com

[36] Practical Strain Gage Measurements. Courtesy of Agilent Technologies Inc., © Agilent Technologies 1999. https://www.omega.co.uk/techref/pdf/StrainGage_Measurement.pdf

[37] R.C. Alderliesten, Fatigue Crack Propagation and Delamination Growth in Glare, PhD thesis, Delft University of Technology, 2005.

[38] J.R. Xiao and J.W. Gillespie JR, A Phenomenological Mohr–Coulomb Failure Criterion for Composite Laminates under Interlaminar Shear and Compression, Journal of Composite Materials, Vol. 41, No. 11/2007, DOI: 10.1177/0021998306067318

[39] Z.M. Zou and H. Lee, A Cohesive zone model taking account of the effect of through-thickness compression, Composites: Part A 98 (2017) 90–98, http://dx.doi.org/10.1016/j.compositesa.2017.03.015

[40] Ahmad S.M. Al-Azzawi, L.F. Kawashita, C.A. Featherston, A modified cohesive zone model for fatigue delamination in adhesive joints: Numerical and experimental investigations, Composite Structures 225 (2019),111114, https://doi.org/10.1016/j.compstruct.2019.111114.

[41] V. Rooijen, Bearing strength characteristics of standard and steel reinforced GLARE®, PhD thesis, Delft University of Technology, 2006.

[42] V. Tvergaard and J.W. Hutchinson, The Relation Between Crack Growth Resistance and Fracture Process Parameters in Elastic-Plastic Solids, Journal of the Mechanics and Physics of Solids,Vol. 40, No. 6. pp. 1377-1397, 1992.

[43] P. Linde, J. Pleitner, H. de Boer, C. Carmone, Modelling and simulation of fibre metal laminates, in: Abaqus Users Conference, Boston, Massachusetts, 25-27 May 2004. URL www.simulia.com/forms/world/pdf2004/LINDE.pdf

[44] S. Sugiman and A.D. Crocombe, The static and fatigue response of metal laminate and hybrid fibre-metal laminate doublers joints under tension loading, Composite Structures, vol. 94, pp. 2937–2951, 2012.

[45] A. Seyed-Yaghoubi and B. Liaw, Experimental and numerical approaches on behavior of Glare 5 beams: Influences of thickness and stacking sequence, in Topics in Modal Analysis II, Volume 6: Proceedings of the 30th IMAC, J. D. C. in: R. Allemang, C. Niezrecki, J. Blough (Eds.), Ed., ed Springer New York, pp. 7-16, 2012.

[46] P. Naghipour, K. Schulze, J. Hausmann and M. Bartsch, Numerical and experimental investigation on lap shear fracture of Al/CFRP laminates, Composites Science and Technology 2012. https://doi.org/10.1016/j.compscitech.2012.07.012

[47] Abaqus/Explicit: Advanced Topics L2.11, Abaqus 2005, SIMULIA™ by Dassault Systèmes®. https://imechanica.org/files/l2-elements.

[48] Abaqus 2005, Abaqus/Explicit: Advanced Topics, Lecture 4 - Contact Modeling. http://ftp.demec.ufpr.br/disciplinas/TM738/l4-contact.pdf

[49] L. Kawashita, A. Kinloch, D. Moore, and J. Williams, The influence of bond line thickness and peel arm thickness on adhesive fracture toughness of rubber toughened epoxyaluminium alloy laminates, International Journal of Adhesion & Adhesives, vol. 28, pp. 199-210, 2008.

[50] K.B. Katnam, A.D. Crocombe, H. Sugiman, H. Khoramishad and I.A. Ashcroft, Static and fatigue failures of adhesively bonded laminate joints in moist environments, International Journal of Damage Mechanics, vol. 20, 2011.

[51] Cytec Engineering Materials, FM® 94 Adhesive Film Technical Data Sheet, Ed., 2010.

[52] M. Hagenbeek, Characterisation of Fibre Metal Laminates under Thermo-mechanical Loadings, PhD thesis, Delft University of Technology, 2005.

[53] Z. Hashin, Failure criteria for unidirectional fibre composites, ASME Journal of Applied Mechanics 47 (2) (1980) 329–334.

[54] Dassault Systemes, Abaqus analysis user's manual version (2019). URL http://www.3ds.com/products-services/simulia/products/ 3dexperience/

Appendix-A

$$G_{IIC} = A_1 + A_2 + A_3 \quad \text{… (a.1)}$$

$$A_2 = G_{IIC} - A_1 - A_3 \quad \text{… (a.2)}$$

$$A_3 = G_{IIC} - A_2 - A_3 \quad \text{… (a.3)}$$

$$A_1 = \frac{{\sigma_{II_{max}}}^2}{2k_{II}} \quad \text{… (a.4)}$$

To calculate area A4 see Figure a.1:

$$A_4 = A_2 + A_3 \quad \text{… (a.5)}$$

$$A_4 = W_1 \,.\, \sigma_{II_{max}} + \frac{(W_2 - W_1).\sigma_{II_{max}}}{2} \quad \text{… (a.6)}$$

$$W_1 = \beta . W_2 \quad \text{… (a.7)}$$

Substitute eq. (a.7) in eq. (a.6) to get area A4:

$$A_4 = \beta . W_2 \,.\, \sigma_{II_{max}} + \frac{(W_2 - \beta . W_2).\sigma_{II_{max}}}{2} \quad \text{… (a.8)}$$

$$A_4 = \beta . W_2 . \sigma_{II_{max}} + W_2 . (1 - \beta) . \frac{\sigma_{II_{max}}}{2} \quad \text{… (a.9)}$$

$$A_4 = W_2 . \sigma_{II_{max}} \left[\beta + \frac{(1-\beta)}{2}\right] \quad \text{… (a.10)}$$

$$A_4 = W_2 . \sigma_{II_{max}} \left[\beta + \frac{1}{2} - \frac{\beta}{2}\right] \quad \text{… (a.11)}$$

$$A_4 = W_2 . \sigma_{II_{max}} \left[\frac{\beta}{2} + \frac{1}{2}\right] \quad \text{… (a.12)}$$

$$A_4 = W_2 . \sigma_{II_{max}} \left[\frac{\beta+1}{2}\right] \quad \text{… (a.13)}$$

Substitute eq. (a.5) in eq. (a.1) to get area A4 as by:

$$A_4 = G_{IIC} - A_1 \quad \text{… (a.14)}$$

Substitute eq. (a.14) in eq. (a.13) as by:

$$G_{IIC} - A_1 = W_2 . \sigma_{II_{max}} \left[\frac{\beta+1}{2}\right] \quad \text{… (a.15)}$$

Substitute eq. (a.4) in eq. (a.15) to get a variable parameter W_2 as by:

$$W_2 = \frac{G_{IIC} - \frac{\left(\sigma_{II\,max}\right)^2}{2 \cdot k_{II}}}{\sigma_{II\,max} \cdot \left(\frac{\beta+1}{2}\right)} \quad \ldots \text{(a.16)}$$

Note, $W_2 = \acute{W}$ used in section 3.1, eq. (13) in this work.

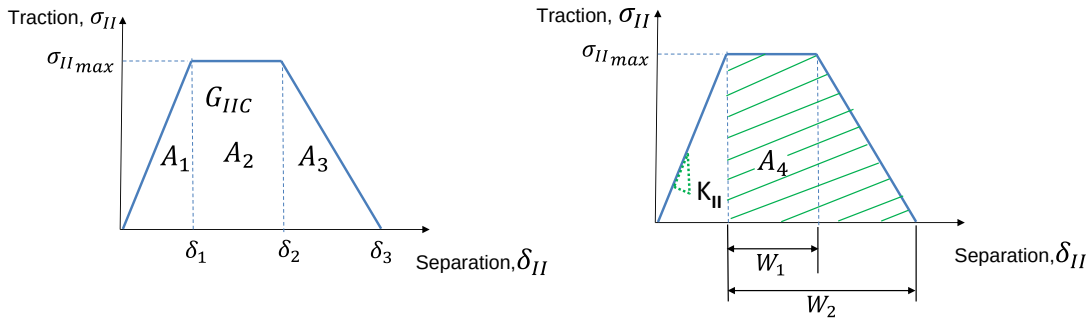

Figure a.1. Constitutive behaviour of trapezoidal based CZM reported by the author in [40].